

Development of a Background Oriented Schlieren Based Wavefront Sensor for Aero-Optics

Abhishek Bichal,^{*} Brian Thurow[†]

Auburn University, Auburn, AL 36849, USA

Abstract

The fundamental principles of Background Oriented Schlieren (BOS) imaging are conducive for the measurement of optical wavefront distortions imposed by turbulent flows. This work explores the initial development of a wavefront sensor based on BOS. The advantages of a BOS based wavefront sensor over a competing device, such as a Shack-Hartmann wavefront sensor, is the ability to measure large aperture wavefronts with potentially high spatial resolution in an economical fashion. An analytical analysis which incorporates the imaging function requirement of the sensor illustrates the ability to measure local wavefront tilts with accuracies on the order of 20 microradians. The analysis finds that under imaging conditions, sensitivity is mainly a function of the lens f-number, which allows the background to be positioned further away from the test section, with the lens focal length only playing a minor role. These ideas were tested using experiments conducted on a cone mounted in a Mach 2.0 wind tunnel. Wavefront measurements agreed qualitatively with the distortion expected from an analytical model of the conical shock's density field. Turbulent boundary layers and Mach wave radiation from the tunnel walls were also detected. Future experiments will calibrate the measurement with a known distortion source. Overall, the concept of a BOS based wavefront sensor is shown to be a valid and viable option for wavefront measurements, particularly for aero-optics studies in medium to large-scale environments.

I. Introduction

The field of aero-optics has received increasing attention as the number of applications involving lasers and other optical devices onboard aircraft,^{1,2} such as targeting and directed energy systems, continues to grow. The effectiveness of these systems depends heavily on the efficiency with which the energy in the laser beam can be delivered to the target. The density-varying (i.e. index-of-refraction) flow field that surrounds the near field of the aircraft, however, causes an adverse effect by distorting the optical wavefront as it passes through the flow field, causing such things as beam jitter, steering and defocus, all of which contribute to a significant reduction in the amount of energy delivered to the target.^{3,4} The study of these phenomena is known as aero-optics.

The integrated effect of these distortions is represented by the point spread function, which is the spatial distribution of intensity of the laser beam at a focal point in the far-field. An undistorted wavefront will result in the familiar airy disc pattern where the majority of energy is concentrated in the airy disc. A distorted wavefront, however, will result in a significant amount of energy being distributed off axis. While one can directly measure the point spread function, it is more useful to measure the wavefront distortion, which is defined as the phase of the wavefront across

^{*} Graduate Student, Department of Aerospace Engineering, AIAA student member.

[†] Associate Professor, Department of Aerospace Engineering, AIAA senior member, corresponding author: thurow@auburn.edu

the beam aperture. Measurement of the wavefront reveals greater detail about the interaction between the turbulent field and the optical wavefront and can distinguish which regions of the flow lead to the greatest amount of distortion.

Traditionally, the distortion of an optical wavefront has been measured using a Shack-Hartmann Wavefront Sensor,^{5,6,7} although earlier works have also described the applications of other wavefront sensors⁸ like the Malley probe,⁹ the digital, photonic, flow diagnostic system¹⁰ etc.. A Shack-Hartmann wavefront sensor uses a lenslet array and a CCD to discretize the incident wavefront and measure the local wavefront tilt. Each lenslet focuses the incident wavefront onto a focal spot on the CCD surface. The location of the spot on the CCD will change depending on the angle of incidence of the incident wavefront. Thus, by measuring the displacement of the spot, one can determine the local tilt of the wavefront and reconstruct the full 2-D wavefront using an array of lenslets. The resolution of the measurement is thus determined by the number of lenslets with the sensitivity dependent on the focal length of each of the lenslets. Although well developed, Shack-Hartmann wavefront sensors suffer from some limitations.¹¹ For one, the spatial resolution is limited by the number of lenslets in the array and the number of pixels on the CCD required in determining the spot position. Second, the size of the measured wavefront is restricted to the size of the CCD, which is generally on the order of 10 – 15 mm. This latter point can be worked around using telescoping optics to reduce the beam aperture to the size of the sensor, but this increases system complexity and cost, and is limited by the size of available optics. In addition, a well collimated laser source is required to produce the incident wavefront upon which the measurement is made. Lastly, a complete system (laser source, collimating optics, sensor and software) can be quite expensive.

For aero-optic measurements in medium to large-scale wind tunnel facilities where the size of the wavefront to be measured is larger (order 2” or greater) and high spatial resolution is needed, these limitations can be difficult to overcome in an economical fashion. In this paper, we present preliminary results in the development of a new wavefront sensor based on the principles of background oriented Schlieren (BOS) imaging. Background oriented Schlieren imaging is a well developed technique that has the advantage that it is relatively simple and cost effective and can be used for the measurement of large aperture wavefronts. It requires only a CCD camera with lens, a random background and a light source to illuminate the background image. In fact, BOS has been demonstrated in real flight tests using a conventional CCD camera,¹² a forest as a background¹³ and the sun as the source of illumination.⁹⁻¹⁴ As will be seen, the image distortion measured in a BOS experiment is directly related to the wavefront distortion, a fact which we seek to exploit to obtain quantitative measurements of the wavefront distortion. In this regards, BOS has the potential to outperform Shack-Hartmann wavefront sensors with respect to spatial resolution, field-of-view and cost. The focus of this paper is on our preliminary efforts to adapt BOS for wavefront measurements. We present the fundamental principles of BOS with respect to wavefront measurements and show preliminary results obtained in a supersonic wind tunnel to demonstrate these capabilities.

II. Background

A. Aero-Optic Wavefront Distortion

The optical properties of a gas are related to the gas density by the Gladstone Dale equation:

$$n(x, y, z, t) = 1 + K\rho(x, y, z, t) \quad (1)$$

where n is the index-of-refraction, ρ is the density of air and K is the Gladstone Dale constant ($2.23 \times 10^{-4} \text{ m}^3/\text{kg}$ for air). In general, and particularly in turbulent flows, density will vary in both space and time resulting in an unsteady, inhomogeneous index-of-refraction field. Light rays propagating through the medium will experience refraction according to:

$$d\varepsilon/ds = \nabla n \quad (2)$$

Where ε is the angle of refraction and s is the direction of light propagation. The total angular deflection of a light ray can be found by integrating along the path, s , of the ray through the medium:

$$\varepsilon = \int_s \nabla n ds \quad (3)$$

The refraction of light rays is closely associated with the optical path length (OPL), ϕ , of a wavefront which is defined as:

$$OPL = \phi = \int_s n ds \quad (4)$$

Combining Eqs. 3 and 4 yields:

$$\varepsilon = \int_s \nabla n ds = \nabla \int_s n ds = \nabla \phi \quad (5)$$

Thus, we see that the total angular refraction of a light ray passing through a turbulent flow field is directly related to the local gradient of the OPL, ϕ .

In aero-optics, one is generally interested in the distortion of a planar wavefront, which can be modeled as a set of initially parallel light rays traveling along the optical axis (generally taken as the z -direction). Furthermore, if the product of tangent of ε and the total path length through the aberrating medium (i.e. the deflection of a ray) is assumed to be small, which is often the case in aero-optic applications, one can approximate $ds = dz$, yielding:

$$\phi = \phi(x, y) = \int n(x, y, z) dz \quad (6)$$

Eq. 6 is generally easier to apply and used to calculate and describe the distortion of a wavefront. Most wavefront measurements are typically reported in terms of the optical path difference (OPD), $\hat{\phi}$, which is defined as:

$$\hat{\phi} = \phi - \bar{\phi} \quad (7)$$

where $\bar{\phi}$ is the average OPL across the beam aperture.

B. Background Oriented Schlieren Imaging

Background Oriented Schlieren (BOS), as implied in the name, is a Schlieren based imaging technique where the refraction of light rays by density gradients in the flow is used as a means of flow visualization. The method varies from traditional Schlieren imaging, however, in that the deflection of light rays is detected by observing the spatial distortion of a background image as opposed to intensity gradients created using a large spherical mirror and a knife edge. While not as sensitive as traditional Schlieren, BOS is more amenable to quantitative analysis, a feature which is exploited in this work.

The basic concept of BOS is illustrated in Fig. 1. A CCD camera (shown here in a pinhole configuration) is used to capture an image of a target placed in the background of the flow field at a distance, s_o , from the camera lens. In the absence of any density gradients, light rays emitted from the center of the background will be imaged onto the center of the CCD, as shown by the solid line. In the presence of an inhomogeneous optical medium, however, light rays

are deflected by an angle, ε , such that the center of the background is displaced by a distance, d_i , on the CCD. Thus, the influence of refraction is to shift the location on the CCD where an image is formed, leading to a distorted image. By imaging a background with high contrast, high frequency content, such as a random dot pattern, image processing algorithms can be applied to measure the local image displacement with subpixel accuracy. We use a PIV based algorithm due to its familiarity, however, optical flow algorithms are also applicable and have the potential to improve the performance described here.

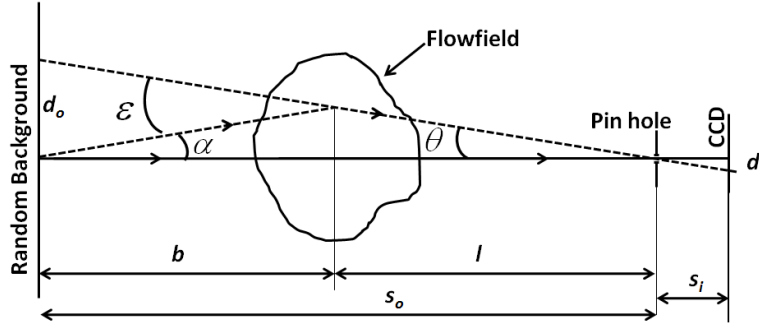


Figure 1. Schematic illustrating basic principles of background oriented Schlieren imaging. A pinhole is shown here instead of a lens for illustrative purposes.

For our application, we must relate the displacement, d_i , observed in the image to the refraction angle, ε . The procedure is fairly straightforward and based on geometrical optics. We note that a key element of this analysis is the assumption of a “thin” flow region relative to the distances l and b such that the effect of the flow can be modeled as thin interface located a distance, l , from the camera lens. We begin by considering the angles in Fig. 1 and noting the relationship:

$$\varepsilon = \alpha + \theta \quad (8)$$

These angles are further related using the trigonometric identity:

$$\tan \varepsilon = \tan(\alpha + \theta) = \frac{\tan \alpha + \tan \theta}{1 - \tan \alpha \tan \theta} \quad (9)$$

The angles α and θ are related to the distance from the flow to the background, b , and from the flow to the camera lens, l , using:

$$b \tan \alpha = l \tan \theta \quad (10)$$

Substituting Eq (10) into (9) for $\tan \alpha$, we arrive at

$$\tan \varepsilon = \frac{\left(\frac{l}{b} + 1\right) \tan \theta}{1 - \frac{l}{b} \tan^2 \theta} \quad (11)$$

For small angles (we measure angles of less than 1 mrad in this work), this reduces to:

$$\varepsilon \approx \tan \varepsilon = \left(1 + l/b\right) \tan \theta \quad (12)$$

From similar triangles, we have

$$\tan \theta = d_i / s_i \quad (13)$$

Which leads to:

$$\varepsilon = (1 + l/b)(d_i / s_i) \quad (14)$$

Where we note that b , l and s_i are constants from the experimental arrangement. Thus, Eq. 14 relates the refraction of a light ray to the measured image displacement for small angular deflections.

C. BOS Wavefront Measurements

The angle, ε , shown in Fig. 1 and in Eq. 14 is the same as that in Eq. 5 providing us with a direct measurement of the wavefront distortion for every point in the image:

$$\varepsilon = \nabla \phi = \left(1 + \frac{l}{b}\right)(d_i / s_i) \quad (15)$$

The full 2-D wavefront, $\phi(x, y)$, can be reconstructed by considering the displacement measured at each location within the image. In this work, image displacements are calculated using PIV algorithms, which have proven to be capable of subpixel accuracy. Once the displacements are known, the local angle of the wavefront is calculated using Eq. 15 and the known values of l , b and s_i from the experimental setup.

To determine the magnitude of the wavefront itself, integration must be performed to reconstruct the distorted wavefront. Previous works on Shack-Hartmann wavefront sensors, which must also reconstruct the wavefront from local tilts, have generally used two methods for the reconstruction problem: discrete gradient based methods and iterative methods.^{15,16} Thurow et. al¹⁷ describe a method whereby the wavefront is discretized and finite difference approximations are applied for each point. The resulting matrix problem is then solved using a singular value decomposition (SVD) approach. This approach becomes computationally extensive with the increasing size of the vector matrix. Another approach, based on iteration, is described by Southwell.¹⁶ In this work, we use the approach described by Southwell, although both methods give similar results.

III. Sensitivity Analysis

In this section, we analytically examine the potential of a BOS wavefront sensor to be used for practical wavefront measurements. The sensitivity of a BOS wavefront sensor is determined by the minimum displacement that can be measured within the image. For this analysis, we model the image sensor as a CCD camera with 6.45 micron square pixels with a resolution of 1376 x 1024 pixels (i.e. Cooke Corp. Sensicam QE) and assume 0.1 pixel accuracy in determination of displacements, which is consistent with the accuracy generally assumed in PIV image analysis. In addition, we also assume that the field-of-view (FOV) of the camera is held constant such that the full test section height of 4" remains in view for all configurations. This latter point is important when comparing our analysis to others found in the literature where the FOV is implicitly dependent on other parameters.

In examining Eq. 15, to first order, sensitivity can be improved by minimizing l/b (i.e. by placing the camera as close to the flow field as possible and moving the background as far away as possible) and by maximizing s_i (choosing a long focal length lens). Practical considerations related to the imaging conditions of the experiment, however, limit one's ability to arbitrarily adjust these parameters. As such, a more detailed analysis is conducted here.

The main constraint that we include in our analysis is the fact that both the test section and the background should be kept nominally in focus. The background must be kept in focus to produce a suitable image for displacement

measurements whereas the test section should be kept in focus such that the corresponding location in the flow field can be properly identified. To satisfy this condition, we model the depth-of-field (DOF) of the imaging lens using the approach outlined in Kingslake.¹⁸ Figure 2 shows the schematic defining the DOF for a given aperture d on the lens. In this figure, the lens imaging condition (i.e. the thin lens equation) is set to focus on the plane located a distance S_f from the lens such that all points originating from this plane form a sharp focal point on the CCD sensor. Rays originating from in front of or behind the focal plane will appear blurred. The DOF is defined by the conical set of rays that fill a spot size, C (also known as the circle of confusion), on the object plane such that the blurred spot is indistinguishable from a spot formed from a point source on the object plane. The size of the spot is typically chosen to correspond to the size of a single pixel; however, this is a rather conservative value. As will be seen, allowing some image blur can have significant benefits to the overall experiment. As can be seen in the figure, the total DOF consists of the region spanning from $S_f - L_1$ to $S_f + L_2$.

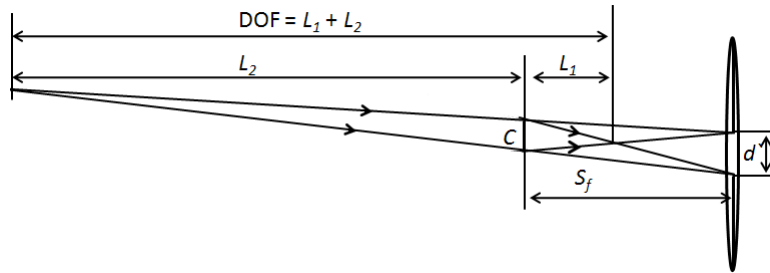


Figure 2. Schematic showing the effect of the lens aperture on the depth of field.

The procedure for calculating the DOF follows the geometry shown in Fig. 2 and is consistent with a geometric optics description of the problem (i.e. we do not include the effects of diffraction, which depend on the lens quality and usually become important for f-numbers of around 16-32). Briefly, we begin with the thin lens equation and associated magnification:

$$1/S_f + 1/S_i = 1/f \quad (16)$$

$$M = S_i/S_f \quad (17)$$

The circle of confusion in object space is related to the pixel size, p , in image space by:

$$C = p/M \quad (18)$$

Using the geometry shown in Fig. 2, it is then straightforward to show (e.g. see Ref.18):

$$L_1 = \frac{CS_f}{d + C} \quad (19)$$

$$L_2 = \frac{CS_f}{d - C} \quad (20)$$

An important parameter that arises from this analysis is the f-number ($f/\#$) of the lens, which is defined as the focal length divided by the lens aperture:

$$f - number = f/\# = \frac{f}{d}$$

Figure 3 shows the effect of the f-number and the focal distance S_f on the DOF for a lens with 75 mm focal length. As can be seen, the DOF increases with increasing S_f and increasing f-number. In the context of this work, both the test section and the background must be placed within the DOF of the lens.

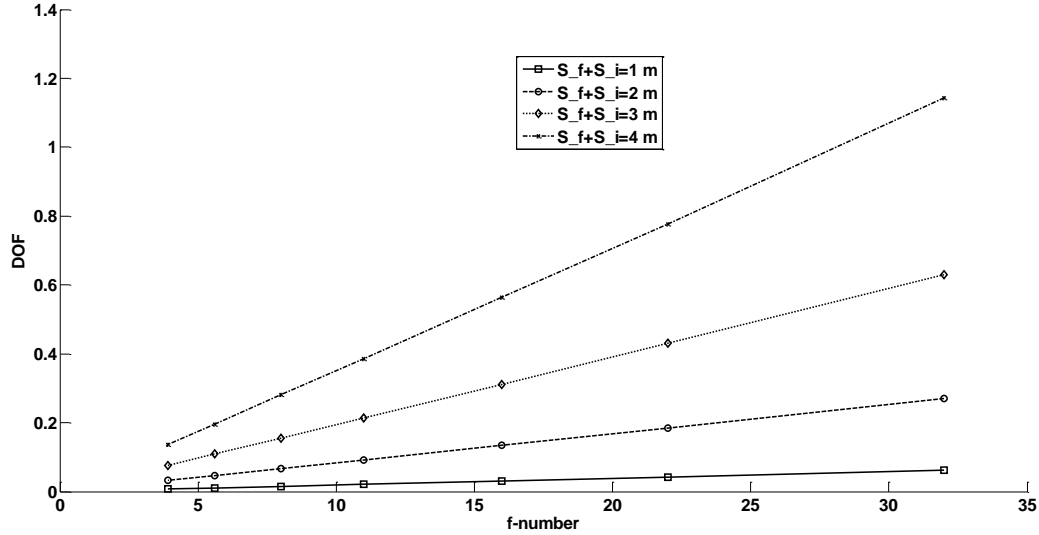


Figure 3. Effect of f-number and the S_f on the depth-of-field of the imaging setup.

To assess the capabilities of this technique in a practical environment, an analytical model that accounts for all of these effects was built in Matlab. As mentioned, both the type of camera and FOV are held constant to simulate the test environment of the Auburn University supersonic wind tunnel, which has a 4" x 4" square test section. Three camera lenses were considered: a 25 mm focal length lens with maximum $f/\#$ of 16, a 50 mm focal length lens with maximum $f/\#$ of 22 and a 75 mm focal length lens with maximum $f/\#$ of 32. In the analysis that follows, we explore the influence of both the focal length and $f/\#$ of the lens on sensitivity. We do so under two imaging conditions. In the first case, we assume that the experiment is set up such that the test section is at the focal plane of the camera and the background is simply placed as far back while staying within the depth of field. The second case corresponds to the focal plane location optimally being adjusted such that the test section lies at the near DOF location (while still maintaining a FOV of 4" at this location) and the background lies at the far DOF location.

Figure 4 illustrates the change in sensitivity (as defined by minimum detectable angle) with focal length for both these cases. The f-number of all three lenses is held fixed at $f/\# = 16$. In both cases, the sensitivity remains almost constant in contrast to increasing with increasing focal length, which is expected from Eq. 15. In the second case, however, the sensitivity is improved though nearly constant across the range of focal lengths considered here. This latter result is somewhat surprising as we expected focal length to play a more important role. It turns out that the increased sensitivity due to focal length is counteracted by the limited DOF and associated increase in the ratio l/b that is forced when one includes the effects of DOF. Optimizing the experimental arrangement to account for these effects balances these competing factors leading to an effective increase in sensitivity keeping the test-section resolution constant. This is a crucial point as longer focal length lenses also require a much longer experimental arrangement, which may not be practical in some lab environments. In addition, a longer arrangement requires a larger background target and higher intensity illumination to cover a larger area. Table 1 lists the various distances associated with this arrangement.

The other factor considered here is the influence of lens $f/\#$ as larger $f/\#$ creates a larger DOF. Figure 5 illustrates the influence this has on the sensitivity for the 75 mm lens. Again, the background is placed at the furthest possible distance away as constrained by the lens DOF, however, the f-number of the lens is adjusted to limit this distance.

The influence is striking with a nearly order of magnitude improvement allowed by operating the lens at the highest f-number possible. Table 2 provides deeper look at the arrangement where the main effect can be seen as a decrease in the l/b ratio as allowed by the increasing DOF. As mentioned, the DOF calculations assume a 1 pixel size circle of confusion. The image analysis procedure used here and based on PIV, however, is expected to remain accurate for even slightly blurred images. In fact, the accuracy of PIV is known to improve if the particles are intentionally blurred such that they are 2-3 pixels in diameter. We also note that PIV correlation algorithm typically use interrogation windows of 16 x 16 pixel size further reducing the demands on spatial resolution. The associated improvement in sensitivity is illustrated in Figure 5 where curves are shown for circles of confusion corresponding to 3 and 5 pixels, respectively. As can be seen, the potential gains in sensitivity are substantial.

We note that increasing the DOF has two limitations. For one, at high $f/\#$'s the image resolution will eventually be limited by diffraction as opposed to the geometrical analysis considered here. Secondly, the amount of light collected decreases exponentially with increasing $f/\#$ such that a brighter illumination source is required. This latter point is somewhat circumvented, however, by the realization that short focal length lenses can yield nearly the same sensitivity thus allowing for the background to be placed much closer to the camera.

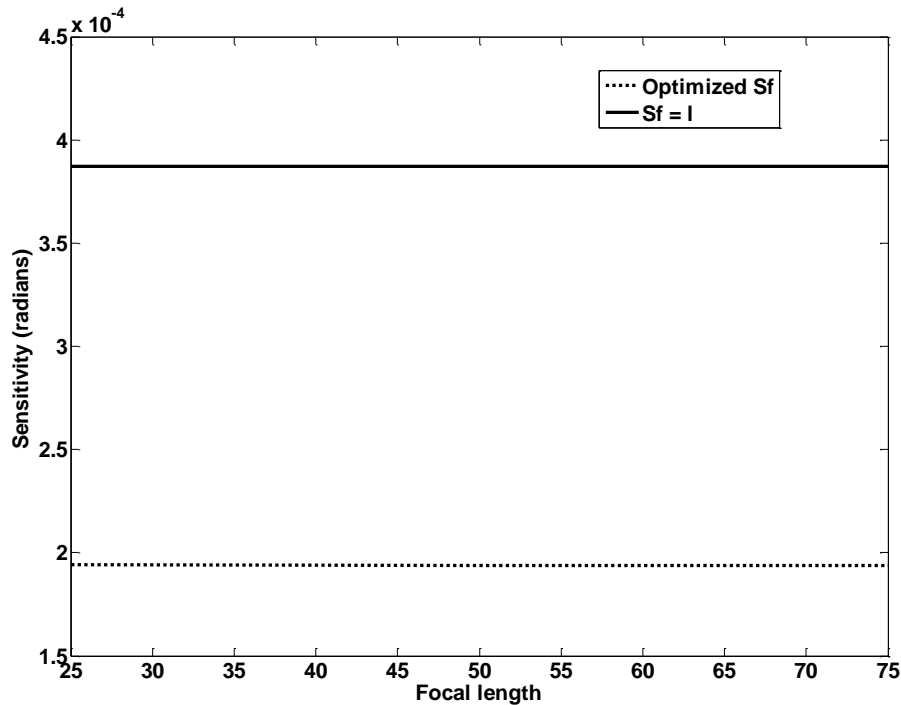


Figure 4. Effect on the sensitivity of the system with varying focal length lenses with the maximum f-number possible for each and keeping the 4" test-section in focus.

Table 1. List of various properties associated with the data shown in Figure 4. Note the increase in overall length with increasing focal length.

Focal length →	25 mm		50 mm		75 mm	
Properties	l	optimized	l	optimized	l	optimized
s_f						
b (m)	0.0269	0.0575	0.0261	0.0537	0.0258	0.0526
$l + b$ (m)	0.4306	0.4596	0.8334	0.8595	1.2367	1.2620

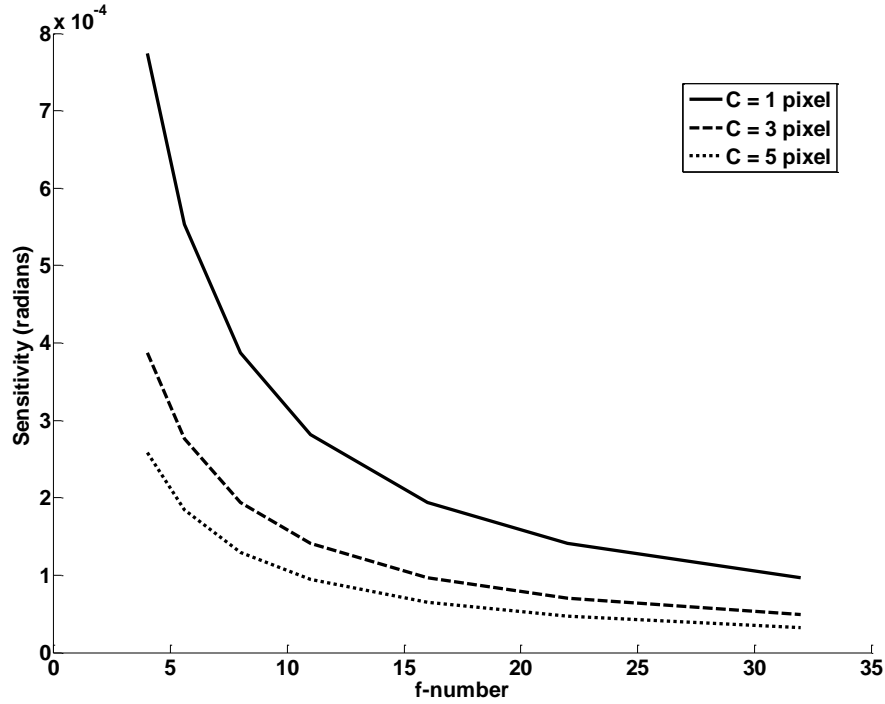


Figure 5. Effect of the f-number on the sensitivity of the system with 75 mm lens with 4” test-section in focus.

Table 2. List of various properties associated with the data shown in Figure 5 for circle of confusion 1 pixel. Note the increase in the ratio l/b with increasing f-number.

f#	4	5.6	8	11	16	22	32
b (m)	0.0127	0.0179	0.0258	0.0357	0.0526	0.0735	0.1098
$l + b$ (m)	1.2233	1.2283	1.2359	1.2456	1.2620	1.2823	1.3177
l/b	94.9646	67.5461	46.9823	33.8962	22.9911	16.4481	10.9956

IV. Test Case: Supersonic Cone

A. Flow Geometry and Analytical Model

To test the ability of BOS to be used for wavefront measurements, an experimental test case was generated using a cone placed in a supersonic flow. This flow was chosen as it creates a stable flow with large enough density gradients to create a measurable wavefront distortion. Perhaps more importantly, an analytical solution to the flow is possible by solving the Taylor-Maccoll equation (Eq.21), thus allowing us to compute the expected wavefront distortion values. Figure 6 shows a schematic of a cone placed in a supersonic flow and the resulting conical shock that originates from the nose. This is a well known problem described by the Taylor-Maccoll equation:

$$\frac{\gamma - 1}{2} \left[V_{\max}^2 - V_r^2 - \left(\frac{dV_r}{d\theta} \right)^2 \right] \left[2V_r + \frac{dV_r}{d\theta} \cot\theta + \frac{d^2V_r}{d\theta^2} \right] - \frac{dV_r}{d\theta} \left[V_r \frac{dV_r}{d\theta} - \frac{dV_r}{d\theta} \left(\frac{d^2V_r}{d\theta^2} \right) \right] = 0 \quad (21)$$

where,

γ , ratio of specific heats of air,

V_r , velocity along the ray,

V_θ , velocity perpendicular to the ray,

θ , is the angle between the axis of the cone and the ray,
 V_{max} , is the square root of two time the stagnation enthalpy.

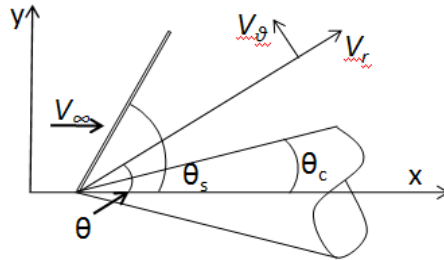


Figure 6. Schematic of the cone model.

Eq. 21, which is given in terms of θ and r was solved numerically to obtain a 2-D function of density. The field was then revolved azimuthally about the cone axis to produce a 3-D function of density for the flow behind the conical shock. The 3-D density data was then converted to index-of-refraction using Eq. 1 and integrated along the z -axis, according to Eq. 6 to simulate the wavefront distortion that would occur due to the presence of the cone. Figure 7 shows the resulting OPD for a 15.5° cone placed in a Mach 2.0 free stream. As can be observed, the conical shock produces a gradual wavefront distortion that increases in the downstream direction. Figure 7 presents the ideal case where there are no disturbances in the free stream and no boundary layers on the wind tunnel windows.

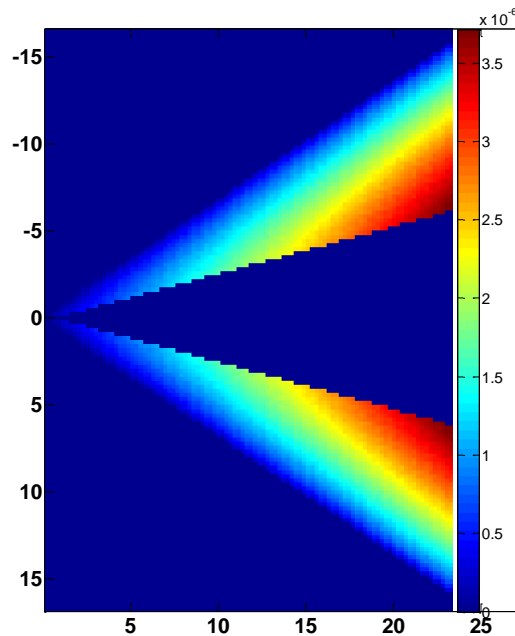


Figure 7. OPD for the analytical model generated in Matlab.

B. Experimental Arrangement

Experiments were conducted in the Auburn University Supersonic wind tunnel facility using a conical geometry nearly identical to that simulated above. The wind tunnel has a 4" x 4" cross-section and is capable of generating Mach numbers between 1.5 and 3.5. The tunnel Mach number was nominally set to Mach 2.0 for the current experiments with a sting mounted cone model placed in the test section. The 23 mm long, 12.77 mm diameter (15.5°) cone was connected to a 12.77 mm diameter cylinder. Figure 8 shows the typical experimental setup for the BOS experiments. The analytical model employed in the sensitivity analysis helped guide the details of the

experimental arrangement. For the experiments discussed herein, space limitations limited us to a 50 mm focal length lens with f-number 22, s_i and s_o are 31.5 and 51 inches respectively. A General Radio 1539A strobeslave strobe light was used for the light source and the images were captured using a Cooke corporation sensicam qe camera at 10 Hz. Both the camera and the strobe light were controlled using a quantum composer digital pulse delay generator. The pulse duration for the strobe light was set at 10 usec and the exposure time on the camera was set at 5 usec. The random background used in the experiments was generated using the algorithm described by Cook et al¹⁹ starting with a 768 X 768 sized random matrix.

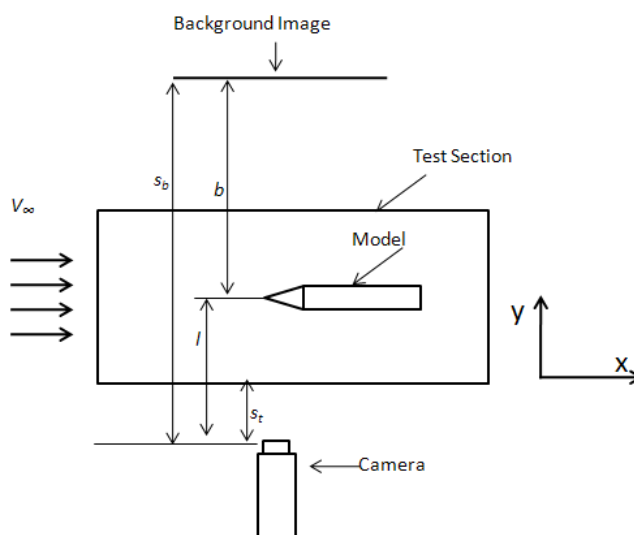


Figure 8. Schematic of experimental arrangement.

Raw images obtained from the experiments were then analyzed with the DPIVB software, PIV analysis software from Innovative Scientific Solutions Inc., Dayton, with 16 pixel X 16 pixel interrogation regions with a 50% overlap. No extra filters were used during the analysis. Deviation vectors thus obtained were analyzed in Matlab to generate the distorted wavefront.

V. Experimental Results

Three types of data were collected during the experiments: a) background image with no flow; b) background with flow but no model; and c) the background with model in the flowfield.

A. No Flow

Several images were acquired under static conditions (i.e. no flow). These images served several purposes. One, the images form the reference image from which displacements are to be calculated. Secondly, these images can be used to assess the noise floor of the measurement system such that the time-dependent effect of lighting intensity, uniformity, camera noise and other non-flow related factors can be assessed. Figure 9 shows a raw image of the background. The illumination is non-uniform and brighter at the center of the image, which is an artifact of the strobe lighting employed in this experiment. We have found enough image information in the dark wings of the image to determine accurate displacement values throughout the entire image. This ability is enhanced by the 12-bit resolution of the camera. PIV analysis of different pairs of flow images gave an average displacement of 0.008 pixels, which is an indication of the stability of the experimental arrangement and small compared to the general assumption of 0.1 pixel accuracy in the PIV based calculations.

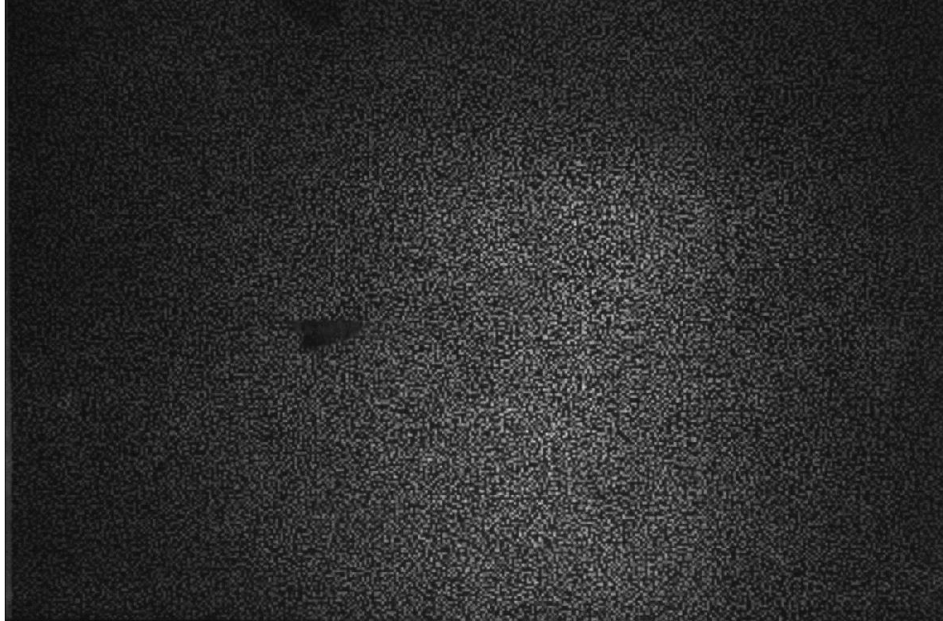


Figure 9. Background image with no flow.

B. Model Free Flow

Ideally, the cone would be the only source of density changes in the flow; however, boundary layers on the tunnel walls and Mach waves associated with supersonic flow will also distort the wavefront passing through the flow. In addition, vibrations can also play a role as the movement of the tunnel windows will create a uniform shift in the background image. To assess the magnitude of these effects, the tunnel was run without the cone model. Figure 10 shows the displacement vectors calculated from one representative image during the tunnel run. The vectors are displayed at 5 times their relative size to emphasize their magnitude, which would be difficult to observe otherwise. In this instance, the average magnitude of displacement is 0.3 pixels. This value was found to decrease in subsequent images, presumably due to the drop in test section pressure that occurs over the duration of a single run. One interesting observation from these images is the appearance of Mach waves originating on the upper surface of the tunnel, a characteristic that is typical in conventional Schlieren images and illustrative of the sensitivity of the technique.

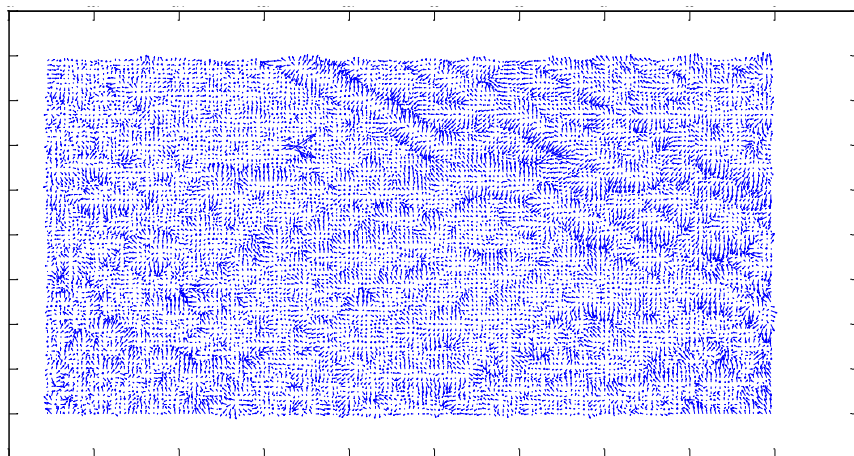


Figure 10. Displacement vectors calculated for Mach 2.0 flow without the cone model present. All vectors shown are 5 times the actual size.

C. Cone Model

Experiments on the cone model were conducted at Mach 2.0. Figure 11 shows an instantaneous (flash duration of 5 microsecond) raw image acquired with the cone in place. Both the background and cone appear to be in focus. This image was correlated with the no-flow image shown above with the instantaneous displacement vectors shown in Figure 12. The appearance of the cone shock is quite apparent. In addition, the formation of an expansion fan at the trailing edge of the cone is also observed as well as another set of shocks associated with fins placed at the rear of the model. In addition, it can be observed that the free stream flow ahead of the shock also experiences displacement due to the turbulent boundary layer formed on the wind tunnel walls, as shown in the previous section.



Figure 11. Raw image of the cone model in Mach 2.0 flow.

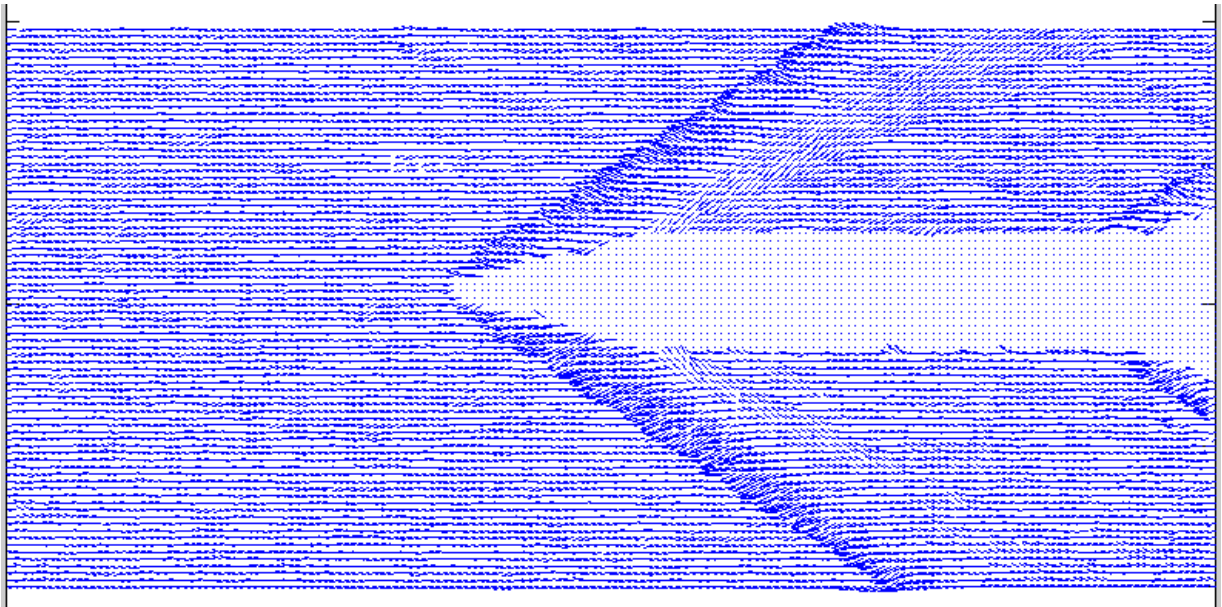


Figure 12. Instantaneous deviation vectors obtained from correlating the Mach 2.0 images with no flow images. All vectors in the image are twice the actual size.

The displacement data was used to reconstruct the wavefront distortion resulting from this flow field as described in Sec. II. The wavefront is shown in Figure 13. Qualitatively, the features are similar to that observed in the analytical model shown in Figure 7. One difficulty in comparing the two images is the influence of the tunnel boundary layers on the wavefront distortion. In an effort to minimize this influence, the wavefront was calculated using only the displacement values found behind the shock. This wavefront is shown in Figure 14. It also qualitatively agrees with that shown in Figure 7. More importantly, the magnitude of the change in OPL across the cone is close to that predicted with the analytical model. It was not possible to determine an average wavefront distortion as the cone model was found to vibrate during experiments. This also has the effect of creating an asymmetric geometry (i.e. the instantaneous position of the cone possessed a non-zero angle of attack) such that the assumptions employed in the analytical cone solution are strictly not valid.

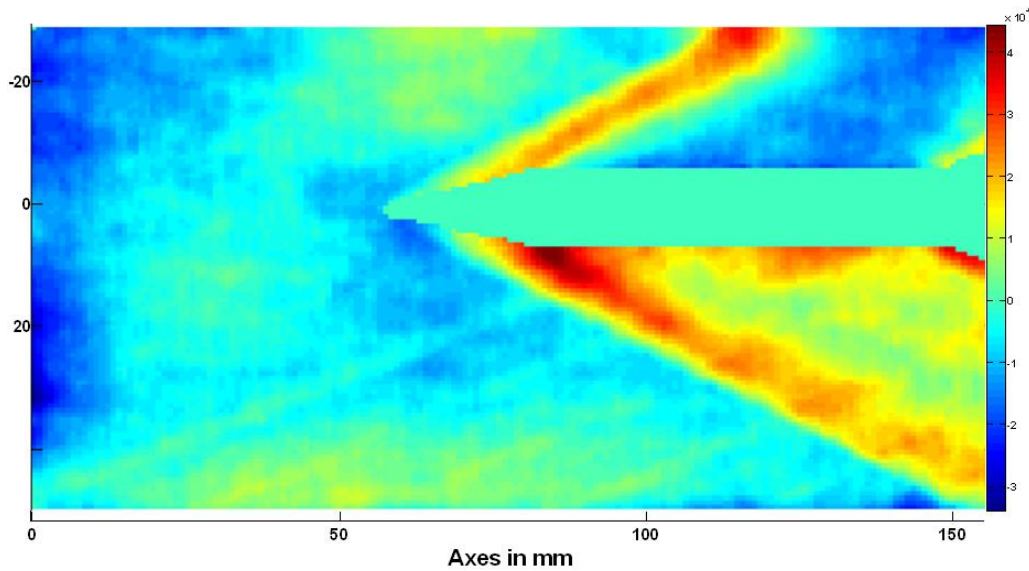


Figure 13. Reconstructed wavefront using the iterative method.

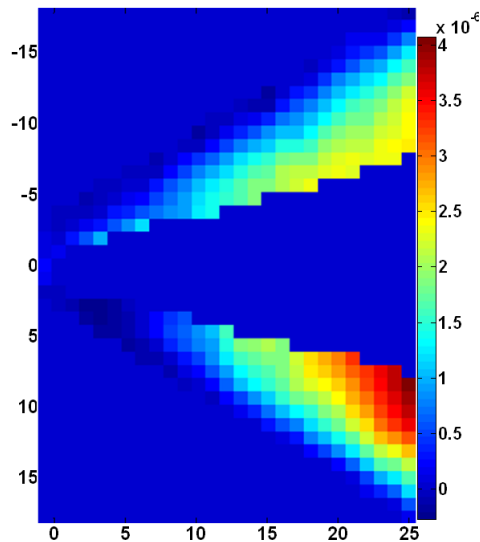


Figure 14. Reconstructed wavefront after the values ahead of the shock are made equal to zero.

VI. Discussion

The results presented here are quite encouraging. After gaining some experience with the general notions of BOS, we have found it quite easy to set up an experiment and obtain results. The experimental results given above appear to agree quite well with what is expected analytically with the shape and magnitude of the conical shock induced wavefront distortion. This gives us a fair amount of confidence in the measurements produced using this technique. Further development, however, will require a more precise calibration which cannot be easily obtained in a fluid dynamic environment due to the presence of turbulent boundary layers and other features which are unsteady. Rather, we are planning to calibrate the technique using a known optical reference, such as a spherical lens whose very function is to accurately distort a wavefront such that it creates a focusing beam.

Such an experiment will allow us to assess the accuracy of various parts of the experimental procedure. For example, we conservatively assume a 0.1 pixel accuracy using the PIV algorithms employed in this study. Recently, however, PIV algorithms have been demonstrated with 0.01 pixel accuracy under well controlled conditions. BOS provides extremely well controlled conditions as the background image is a static target not prone to particle drop out and other problems typically associated with PIV. Furthermore, these conditions open up the possibility of applying optical flow algorithms²⁰ which can be even more accurate than PIV and have the potential to improve spatial resolution (to order 3-5 pixel diameter). Currently, the spatial resolution is limited by the interrogation window (typically 16 x 16 pixels) used to determine the displacement in the PIV algorithm.

Perhaps the most relevant discussion point is to compare the BOS wavefront measurements with those obtained with a Shack-Hartmann wavefront sensor. At this point in time, we do not possess a sensor to make a direct comparison, which would be ideal; however, we can offer several generic thoughts. First, the accuracy of a Shack-Hartmann wavefront sensor is determined by the displacement of a focal spot formed by an array of micro-lenses. Interestingly, this can be quantified using Eq. 15 by taking $s_i=f$ and $b=\infty$. In other words, a Shack-Hartmann wavefront sensor acts in the same fashion as the BOS wavefront sensor described here in the limit of a background of point sources placed infinitely far away. This analogous behavior is quite encouraging. The main disadvantage to a BOS based sensor is the finite value of l/b that is a consequence of the limited DOF of the imaging arrangement. As can be seen in the sensitivity analysis, an optimized arrangement can reduce the value of l/b considerably such that the sensitivity of a Shack-Hartmann sensor can be approached. An open question, with respect to sensitivity, is whether one can locate the center of spot more accurately than one can calculate the displacement between a pair of images. This is still to be determined.

The main advantage of BOS; however, is the ease in which the experiment can be set up and scaled to various sizes. As mentioned in the introduction, the experimental arrangement is rather simple as one only needs a CCD camera with appropriate imaging lens, a random background target and a suitable illumination source to provide intensity and limit exposure time. The size of wavefront being sampled is determined simply by the field-of-view of the camera. Shack-Hartmann wavefront sensors, on the other hand, require a well collimated laser source to produce finite focal spots and have a spatial resolution limited by the resolution of the micro-lens array, which must be sized according to the CCD size. As such, telescoping optics are necessary to sample a wavefront larger than the CCD, which means that special optics are necessary for different experiments and that large aperture wavefront measurements may not be possible or cost prohibitive.

VII. Conclusions and Future Work

The use of BOS imaging is shown to be a viable technique for wavefront measurements. An analytical sensitivity analysis of the BOS wavefront sensor showed accuracy of measuring deviation vectors up to 20 micro-radians. It is found that the sensitivity of the BOS wavefront sensor is a function of the focal length and f-number of the lens when restricted by the field-of-view and DOF of the imaging system. In an optimized configuration taking

advantage of the full DOF available, it is found that the sensitivity only mildly depends on focal length and primarily depends on the lens $f/\#$, which should be as large as possible.

An analytical Mach 2.0 flow over a cone was generated to obtain an analytical wavefront distortion. Experiments were also conducted at Mach 2.0 in the supersonic wind tunnel. The deformed wavefront was generated from the experimental data. When compared with the wavefront generated from the analytical procedure, both wavefronts agree qualitatively. This shows the practical applicability of the BOS technique as a wavefront sensor. Simple equipment like the stable light source, camera and any regular lens makes BOS a low cost wavefront sensor.

A detailed and more specific comparison of the BOS wavefront sensor to the Shack-Hartmann sensor is planned along with a further error analysis and the study of limitations of the technique. Application of the BOS wavefront sensing to more generalized turbulent flows, like flow behind the hemisphere in transonic flow, are also planned.

¹ Stathopoulos, F., Constantinou, P., "Impact of Aircraft Boundary Layer on Laser Beam Propagation", International Workshop on Satellite and Space Communications (IWSSC), 1-3 Oct., 2008, IEEE.

² Conrad, R. A., Murphy, R. J., Williams T. H., Wilcox, W. E., Michael, S., Roth, J. M., "Experimental comparison of tracking algorithms in the presence of aircraft boundary-layer distortions for emulated free-space laser communication links," *Applied Optics*, Vol. 48, A98-A106, 2009.

³ Stathopoulos, F., Constantinou, P., Panagopoulos, A. D., "Impact of Various Flow-Fields on Laser Beam Propagation", International Workshop on Satellite and Space Communications (IWSSC), 9-11 Sep., 2008, IEEE.

⁴ Dimotakis, P. E., Catrakis, H. J., Fourchette, D. C., "Flow structure and optical beam propagation in high-Reynolds-number gas-phase shear layers and jets", *Journal of Fluid Mechanics*, Vol. 433, pp 105-134, Cambridge University Press, United Kingdom, 2001.

⁵ Neal, D. R., Hedlund, E., Lederer, M., Collier, A., Spring, C., Yanta, B., "shack-Hartmann Wavefront Sensor Testing of Aero-Optic Phenomena", American Institute of Aeronautics and Astronautics, 1998.

⁶ Lena, P., "Adaptive optics: a breakthrough in astronomy", *Experimental Astronomy*, Springer, 2009.

⁷ Schwiegerling, J., Neal, D. R., "Historical Development of the Shack-Hartman Wavefront Sensor".

⁸ Jumper, E. J., Fitzgerald, E. J., "Recent Developments in Aero-optics," *Progress in Aerospace Sciences*, Vol. 37, pp 299-339, 2001.

⁹ Malley, M. M., Sutton, G. W., Kincheloe, N., "Beam-Jitter Measurements of Turbulent Aero-optical Path Differences," *Applied Optics*, Vol. 31, No. 22, 1 August 1992.

¹⁰ Trolinger, J., "High Speed Digital Wavefront Sensing for Aero-Optics and Flow Diagnostics," *20th International Congress on Instrumentation in Aerospace Simulation Facilities (ICIASF)*, IEEE, Göttingen Germany, 2003.

¹¹ Primot, J., Rousset, G., Fontanella, J. C., "Deconvolution from wave-front sensing: a new technique for compensating turbulence-degraded images", *Journal of Optical Society of America*, Vol. 7, Issue 9, pp 1598-1608, 1990.

¹² Raffel, M., Richard, H., Meier, G. E. A., "On the Applicability of Background Oriented Optical Tomography for Large Scale Aerodynamic Investigations," *Experiments in Fluids*, Vol. 28, 2000, pp 477-481.

¹³ Sommersel, O. K., Bjerketvedt, D., Christensen, S. O., Kerst, O., Vaagsaether, K., "Application of Background Oriented Schlieren for Quantitative Measurement of Shock Waves from Explosions," *Shock Waves* [published online 22 May 2008], Vol. 18, pp 291-297.

¹⁴ Settles, G. S., "Schlieren and Shadowgraph Imaging in the Great Outdoors," *Proceeding of PSFPIV-2*, Honolulu, USA, May 16-19, 1999.

¹⁵ Bradsley, J. M., "Wavefront Reconstruction Methods for Adaptive Optics Systems on Ground-Based Telescopes," Work done at University of Helsinki, Finland, University of Montana Faculty Exchange Program, 2006-07.

¹⁶ Southwell, W. H., "Wave-Front Estimation from Wave-Front Slope Measurements," *Journal of Optical Society of America*, Vol. 70, No. 8, August 1980.

¹⁷ Thurow, B. et. al., "Simultaneous MHz Rate Flow Visualization and Wavefront Sensing for Aero-Optics," *41st AIAA Aerospace Science Meeting and Exhibit*, Reno, Nevada, January 6-9, 2003.

¹⁸ Kingslake, R., *Optics in Photography*, SPIE Optical engineering Press, Bellingham, Washington, USA, 1992, Chap. 5, pp. 84-88.

¹⁹ Cook, R. L., DeRose, T., "Wavelet Noise," Pixar Animation Studios [online], URL: <http://graphics.pixar.com/library/WaveletNoise/paper.pdf> [cited 14 June 2010].

²⁰ Atcheson, B., Heidrich, W., "An Evaluation of Optical Flow Algorithms for Background Oriented Schlieren Imaging," *Experiments of Fluids*, Vol. 46, pp 467-476, 2009.